Small-Signal Impedance Modeling and Analysis of Variable-Frequency AC Three-Stage Generator for More Electric Aircraft

Shuang Wang, *Student Member, IEEE*, Xinbo Ruan, *Fellow, IEEE*, Yuying He, *Member, IEEE*, Zhiheng Lin, *Student Member, IEEE*, Chengxiang Zhang, *Student Member, IEEE*, and Donghua Wu

***Abstract*—With the penetration of power electronics in more electric aircraft (MEA) power systems, the number of constant power loads continues increasing and the characteristics of negative resistance of their terminal impedances tend to impair the system stability. The variable-frequency ac (VFAC) three-stage generator (TSG) is the main power supply of the MEA VFAC power system, and it is essential to establish its small-signal impedance model for analyzing the system stability. In this article, an accurate small-signal impedance model of the VFAC-TSG is established under the synchronous *d-q* frame. On this basis, the terminal characteristics of the VFAC-TSG in open-loop and closed-loop modes are analyzed in detail. Furthermore, the impacts of the rotation speed and digital control delay on the terminal characteristics are demonstrated. Finally, the experimental results from a hardware-in-the-loop platform are provided to verify the accuracy of the proposed impedance model and the correctness of the theoretical analysis.**

***Index Terms*—*D-Q* frame, more electric aircraft (MEA), small-signal impedance model, three-stage generator (TSG), variable-frequency ac (VFAC).**

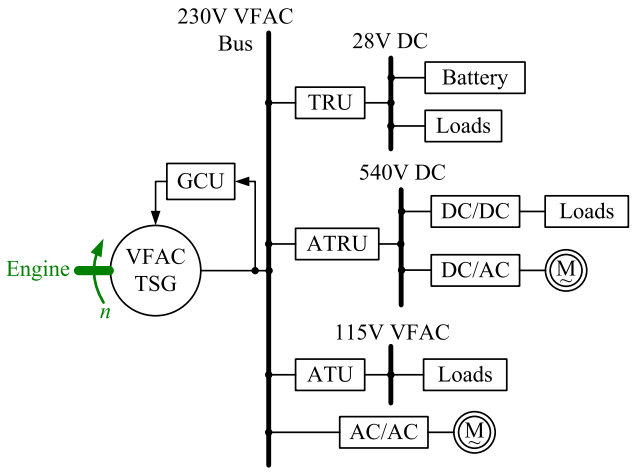

Fig. 1. Simplified MEA VFAC power system.

I. Introduction

In AIRCRAFT, the secondary energy sources, including electrical, hydraulic, and pneumatic energy, are generated by the engine. In recent years, hydraulic and pneumatic energy are gradually replaced with electrical energy to reduce gas emissions, decrease costs, and improve reliability. Accordingly, electrical energy becomes the majority of the secondary energy sources, and the aircraft is called the more electric aircraft (MEA) [1], [2].

Manuscript received 8 February 2022; revised 26 April 2022 and 22 June 2022; accepted 5 August 2022. Date of publication 15 August 2022; date of current version 10 October 2022. Recommended for publication by Associate Editor M. Molinas. *(Corresponding author: Xinbo Ruan.)*

Shuang Wang, Xinbo Ruan, Zhiheng Lin, and Chengxiang Zhang are with the Center for More-Electrical-Aircraft Power System, College of Automation Engineering, Nanjing University of Aeronautics and Astronautics, Nanjing 211106, China (e-mail: wshuang@nuaa.edu.cn; ruanxb@nuaa.edu.cn; lzh@nuaa.edu.cn; mrzcx@nuaa.edu.cn).

Yuying He is with the College of Energy and Electrical Engineering, Hohai University, Nanjing 211100, China (e-mail: heyuying@ieee.org).

Donghua Wu is with the Aviation Key Laboratory of Science and Technology on Aerospace Power System, Shaanxi Aero Electric Co., Ltd., Xi'an 710000, China (e-mail: dhwu2@126.com).

Color versions of one or more figures in this article are available at https://doi.org/10.1109/TPEL.2022.3198545.

Digital Object Identifier 10.1109/TPEL.2022.3198545

In the early days, the onboard electric loads are used for basic functions such as lighting, heating, and flight controls, and the low-voltage dc power system was adopted [3]. Later, more and more electric loads (e.g., deicing and environmental control) are introduced. In this scenario, a higher voltage level is required to reduce the cabling weight and loss. However, higher voltage systems present concerns related to safety and risk, especially for the dc systems dependent on electromechanical commutation [4]. Thus, the dc power system is gradually replaced by the ac power system coupled with the constant speed drives (CSD) [5]. It is also termed the constant speed constant frequency power system, which has ever been a common choice for decades. However, the CSD is a complex hydromechanical gearbox with low efficiency in delivering power from the engine to the generator [6]. This stimulated the progress on feasible alternatives, and the era of the variable-frequency ac (VFAC, 360–800 Hz) power system without the heavy CSD was launched. At present, the VFAC power system has been widely applied to the state-of-art MEAs (e.g., Boeing 787 and Airbus A380) [7], [8], [9], [10].

Fig. 1 illustrates a typical MEA VFAC power system. The three-stage generator (TSG), which is coupled to the engine by a gearbox with a constant gear ratio, is the most popular ac generator in MEA. This popularity is due to its inherent

safety since the excitation can be instantaneously removed through direct control of the field to de-energize the machine [4], [11]. On the distribution and consumption side, there are various power converters and motor drive loads, which behave as constant power load (CPL) when tightly controlled [12]. The real part of the CPL impedance is negative, posing a risk of system instability [13], [14], [15], [16]. Hence, it is highly significant to analyze the stability of the MEA VFAC power system.

Generally, there are two basic methods for analyzing system stability, namely the time-domain analysis method and the frequency-domain analysis method [17]. The former is based on the state-space model and evaluates the system stability by listing the state-space equations and then solving their eigenvalues. However, the MEA power system contains a large number of loads, which indicates that the orders of the system state-space equations are high, leading to complex analysis and extensive calculations [18], [19], [20], [21], [22]. In addition, the electrical loads have different operating conditions during the flight of aircraft, and the state-space models of the system should be established under all the operating conditions. Therefore, although this method is effective, it is unappealing for the stability analysis of the MEA power system.

In contrast, the frequency-domain analysis method based on the impedance model is more promising. By regarding each device connected to the voltage bus as an independent subsystem, the stability of the whole system can be predicted by the impedances of each subsystem [23]. This method can clearly tell how to reshape the impedance of each subsystem to improve the system's stability. Besides, adding/removing a load or changing its operating mode only affects one impedance element in the whole impedance network, whose effects on the system stability can thus be easily assessed. Owing to these merits, this method has been widely used in high-speed railway systems [24], [25], grid-tied converters [26], [27], and MEA power systems [28], [29], [30], [31]. Regarding the MEA, the impedance-based stability analysis of the potential permanent magnet synchronous generator-based dc microgrid for future MEA is conducted in [28], [29], and [30], and the impedance model of the alternative induction generator in the VFAC power system is built to address its self-excitation issue in [31]. Yet, so far, the systematic impedance model of the popular MEA VFAC power system is still lacking in the existing literature. Considering that the TSG is the main power supply of the VFAC power system, its accurate impedance modeling and analysis are of great significance.

To fill this gap, this article is dedicated to establishing the small-signal impedance model of the VFAC-TSG and revealing how the key parameters affect its terminal characteristics. The outcomes of this work are concluded as follows.

1) The small-signal impedance model of the VFAC-TSG is established under the synchronous *d-q* frame.
2) The terminal characteristics of the VFAC-TSG in the open-loop and closed-loop modes are analyzed in detail.
3) The impacts of the rotation speed and digital control delay on the terminal characteristics are demonstrated.

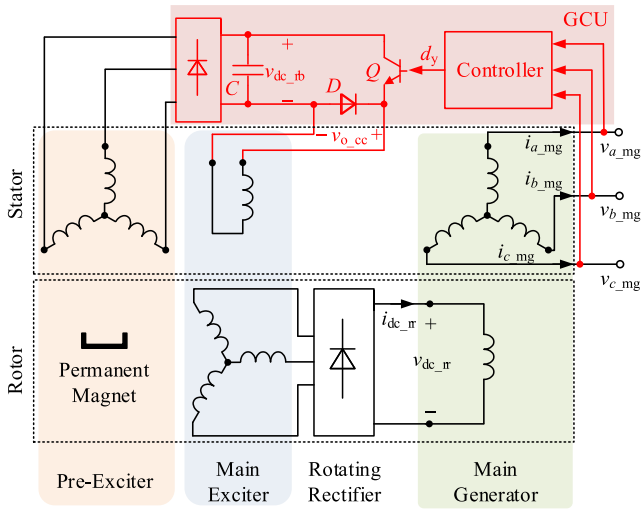

Fig. 2. Structure of the VFAC-TSG.

This work is a foundation for future research on VFAC-TSG, which can help evaluate the system stability and design the controller parameters for gaining optimal performance. The rest of this article is organized as follows. In Section II, the operating principle of the VFAC-TSG is introduced. In Section III, the small-signal models of the main generator, main exciter, pre-exciter, rotating rectifier, and generator control unit (GCU) are derived under the synchronous *d-q* frame, which are then integrated into the small-signal impedance model of the VFAC- TSG. In Section IV, the terminal characteristics of the VFAC-TSG in open-loop and closed-loop modes are analyzed, and the effects of the rotation speed and digital control delay are demonstrated. In Section V, the experimental results from the hardware-in-the-loop platform of the VFAC-TSG are provided to verify the accuracy of the proposed impedance model and the correctness of the theoretical analysis. Finally, Section VI concludes this article.

II. Operating Principle of the VFAC-TSG

Fig. 2 shows the structure of the VFAC-TSG, including the pre-exciter, main exciter, main generator, and rotating rectifier, GCU. The pre-exciter is a permanent magnet synchronous generator, whereas the main generator and the main exciter are electrically excited synchronous generators.

The pre-exciter serves as the power supply for excitation, whose armature winding is located on the stator and connected to the three-phase rectification bridge to feed the chopper circuit in the GCU. The chopper circuit regulates the field current to the main exciter. The armature winding of the main exciter is located on the rotor and provides the main generator's field current through the rotating rectifier. When the rotation speed or load of the VFAC-TSG changes, the field current of the main generator is regulated by adjusting the field current of the main exciter. Thereby, the output voltage of the main generator is regulated.

III. Small-Signal Model of the VFAC-TSG

In this section, the above-mentioned five parts of the VFAC-TSG are modeled in sequence and then integrated to obtain the small-signal model of the VFAC-TSG.

A. Modeling of Main Generator and Main Exciter

The small-signal modeling of the electrically excited synchronous generators (i.e., the main generator and the main exciter) is elaborated as follows.

Ignoring the impacts of the damper winding and converting the physical quantities of the field winding to the ones of the armature winding, the voltage equations under the synchronous d-q frame can be expressed as [32]

$$\begin{cases} v_d(t) = -\omega\psi_q(t) + \frac{d}{dt}\psi_d(t) + R_\mathrm{a} i_d(t) \\ v_q(t) = \omega\psi_d(t) + \frac{d}{dt}\psi_q(t) + R_\mathrm{a} i_q(t) \\ v_\mathrm{f}(t) = \frac{d}{dt}\psi_\mathrm{f}(t) + R_\mathrm{f} i_\mathrm{f}(t) \end{cases} \tag{1}$$

where v_d, i_d, and ψ_d are the d-axis armature voltage, current, and flux linking, respectively, and v_q, i_q, and ψ_q are the q-axis ones. v_f, i_f, and ψ_f are the field voltage, current, and flux linking, respectively, R_a is the armature resistance, R_f is the field resistance, and ω is the electrical angular frequency.

The flux linking equations can be expressed as

$$\begin{cases} \psi_d(t) = L_{md}\left(i_d(t) + i_\mathrm{f}(t)\right) + L_\mathrm{l} i_d(t) \\ \psi_q(t) = L_{mq} i_q(t) + L_\mathrm{l} i_q(t) \\ \psi_\mathrm{f}(t) = L_{md}\left(i_d(t) + i_\mathrm{f}(t)\right) + L_\mathrm{lf} i_\mathrm{f}(t) \end{cases} \tag{2}$$

where, L_{md} and L_{mq} are the d- and q-axis mutual inductance, respectively, L_l is the armature inductance, and L_lf is the field leakage inductance.

Substituting (2) into (1) yields

$$\begin{cases} v_d(t) = R_\mathrm{a} i_d(t) + L_d\frac{di_d(t)}{dt} + L_{md}\frac{di_\mathrm{f}(t)}{dt} - \omega L_q i_q(t) \\ v_q(t) = R_\mathrm{a} i_q(t) + L_q\frac{di_q(t)}{dt} + \omega L_{md} i_\mathrm{f}(t) + \omega L_d i_d(t) \\ v_\mathrm{f}(t) = R_\mathrm{f} i_\mathrm{f}(t) + L_\mathrm{f}\frac{di_\mathrm{f}(t)}{dt} + L_{md}\frac{di_d(t)}{dt} \end{cases} \tag{3}$$

where $L_d = L_{md} + L_\mathrm{l}$ is the d-axis armature inductance, $L_q = L_{mq} + L_\mathrm{l}$ is the q-axis armature inductance, and $L_\mathrm{f} = L_{md} + L_\mathrm{lf}$ is the field inductance.

Imposing small-signal perturbation to the variables v_d, v_q, i_d, i_q, v_f, and i_f in (3) and manipulating gives

$$\hat{\boldsymbol{v}}_{\boldsymbol{dq}}(\boldsymbol{s}) = \boldsymbol{G}_{\boldsymbol{vdq-idq}}(\boldsymbol{s})\hat{\boldsymbol{i}}_{\boldsymbol{dq}}(\boldsymbol{s}) + \boldsymbol{G}_{\boldsymbol{vdq-if}}(\boldsymbol{s})\hat{i}_\mathrm{f}(s) \tag{4}$$

$$\hat{i}_\mathrm{f}(s) = \boldsymbol{G}_{\boldsymbol{if-idq}}(\boldsymbol{s})\hat{\boldsymbol{i}}_{\boldsymbol{dq}}(\boldsymbol{s}) + G_{if-vf}(s)\hat{v}_\mathrm{f}(s) \tag{5}$$

where $\boldsymbol{v_{dq}} = [v_d\ v_q]^T$, $\boldsymbol{i_{dq}} = [i_d\ i_q]^T$, and $\boldsymbol{G_{vdq\text{-}idq}(s)}$, $\boldsymbol{G_{vdq\text{-}if}(s)}$, $\boldsymbol{G_{if\text{-}idq}(s)}$, and $G_{if\text{-}vf}(s)$ are expressed as

$$\boldsymbol{G}_{\boldsymbol{vdq-idq}}(\boldsymbol{s}) = \begin{bmatrix} R_\mathrm{a} + sL_d & -\omega L_q \\ \omega L_d & R_\mathrm{a} + sL_q \end{bmatrix} \tag{6}$$

$$\boldsymbol{G}_{\boldsymbol{vdq-if}}(\boldsymbol{s}) = \begin{bmatrix} sL_{md} \\ \omega L_{md} \end{bmatrix} \tag{7}$$

$$\boldsymbol{G}_{\boldsymbol{if-idq}}(\boldsymbol{s}) = \begin{bmatrix} -\frac{sL_{md}}{R_\mathrm{f} + sL_\mathrm{f}} & 0 \end{bmatrix} \tag{8}$$

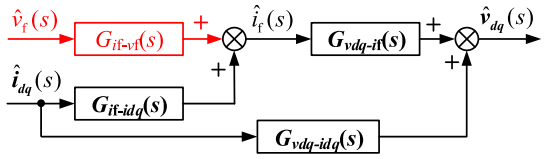

Fig. 3. Small-signal model of the main generator and the main exciter.

$$G_{if-vf}(s) = \frac{1}{R_\mathrm{f} + sL_\mathrm{f}}. \tag{9}$$

According to (4) and (5), the small-signal models of the main generator and the main exciter can be obtained, as shown in Fig. 3.

B. Modeling of the Rotating Rectifier

Define $v_{\mathrm{dc\_rr}}$ and $i_{\mathrm{dc\_rr}}$ as the output voltage and output current of the rotating rectifier, respectively, and v_{d_me}, v_{q_me}, i_{d_me}, and i_{q_me} are the armature voltages and currents of the main exciter under the synchronous d-q frame, we have [33]

$$v_{\mathrm{dc\_rr}}(t) = \frac{3\sqrt{3}}{\pi}\left(v_{d\_\mathrm{me}}(t)\sin\delta(t) + v_{q\_\mathrm{me}}(t)\cos\delta(t)\right) \tag{10}$$

$$i_{d\_\mathrm{me}}(t) = \frac{2\sqrt{3}}{\pi} i_{\mathrm{dc\_rr}}(t)\sin\left(\delta(t) + \varphi\right) \tag{11}$$

$$i_{q\_\mathrm{me}}(t) = \frac{2\sqrt{3}}{\pi} i_{\mathrm{dc\_rr}}(t)\cos\left(\delta(t) + \varphi\right) \tag{12}$$

where φ is the angle of the armature current behind the armature voltage of the main exciter, and δ is the power angle of the main exciter, expressed as

$$\delta(t) = \operatorname{atan}\frac{v_{d\_\mathrm{me}}(t)}{v_{q\_\mathrm{me}}(t)}. \tag{13}$$

Imposing small-signal perturbation to the variables v_{d_me}, v_{q_me}, i_{d_me}, i_{q_me}, $v_{\mathrm{dc\_rr}}$, $i_{\mathrm{dc\_rr}}$, and δ in (10)–(13), and manipulating, gives

$$\hat{v}_{\mathrm{dc\_rr}}(s) = \boldsymbol{K_v}\hat{\boldsymbol{v}}_{\boldsymbol{dq\_me}}(\boldsymbol{s}) \tag{14}$$

$$\hat{\boldsymbol{i}}_{\boldsymbol{dq\_me}}(\boldsymbol{s}) = \boldsymbol{Y_0}\hat{\boldsymbol{v}}_{\boldsymbol{dq\_me}}(\boldsymbol{s}) + \boldsymbol{K_i}\hat{i}_{\mathrm{dc\_rr}}(s) \tag{15}$$

where the transfer matrices $\boldsymbol{K_v}$, $\boldsymbol{K_i}$, and $\boldsymbol{Y_0}$ are expressed as

$$\boldsymbol{K_v} = \begin{bmatrix} \frac{3\sqrt{3}}{\pi}\sin\delta_\mathrm{N} & \frac{3\sqrt{3}}{\pi}\cos\delta_\mathrm{N} \end{bmatrix} \tag{16}$$

$$\boldsymbol{K_i} = \begin{bmatrix} \frac{2\sqrt{3}}{\pi}\sin\left(\delta_\mathrm{N} + \varphi\right) & \frac{2\sqrt{3}}{\pi}\cos\left(\delta_\mathrm{N} + \varphi\right) \end{bmatrix}^T \tag{17}$$

$$\boldsymbol{Y_0} = \frac{1}{\sqrt{V_{d\_\mathrm{me}}^2 + V_{q\_\mathrm{me}}^2}}\begin{bmatrix} I_{q\_\mathrm{me}}\cos\delta_\mathrm{N} & -I_{q\_\mathrm{me}}\sin\delta_\mathrm{N} \\ -I_{d\_\mathrm{me}}\cos\delta_\mathrm{N} & I_{d\_\mathrm{me}}\sin\delta_\mathrm{N} \end{bmatrix} \tag{18}$$

with V_{d_me}, V_{q_me}, I_{d_me}, and I_{q_me} are the steady-state armature voltage and current of the main exciter on the d- or q-axis, and δ_N is the steady-state power angle of the main exciter.

According to (14) and (15), the model of the rotating rectifier can be derived, as shown in Fig. 4.

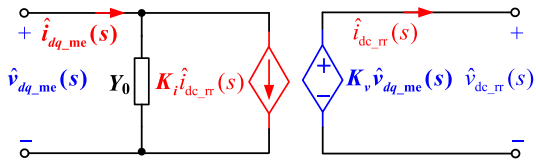

Fig. 4. Small-signal model of the rotating rectifier.

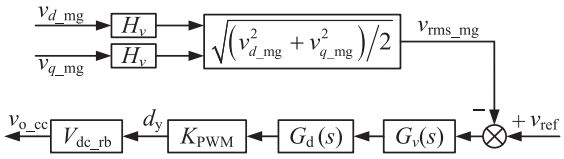

Fig. 5. Control diagram of the GCU.

C. Modeling of the GCU

Fig. 5 shows the control diagram of the GCU, where v_{d_mg} and v_{q_mg} are the voltages of the main generator under the synchronous d-q frame, and they are sampled with the sense gain of H_v. The root mean square (rms) value of the sensed voltages is calculated as v_{rms_mg}, which is then compared with the voltage reference v_{ref}. The error is sent to the voltage regulator $G_v(s)$, whose output serves as the modulated signal. Via a digital pulsewidth modulator (PWM), the duty cycle d_y for the power switch is generated. In the digital control process, the control delay $G_d(s) = e^{-1.5sTs}$ is introduced, where T_s is the sampling period [34]. $K_{PWM} = 1/V_{tri}$ is the transfer function from the modulated wave to the duty cycle, where V_{tri} is the amplitude of the triangular carrier.

Recalling Fig. 2, the chopper circuit in the GCU is fed by the pre-exciter through the three-phase rectification bridge. The voltage equation of the pre-exciter is [29]

$$\begin{cases} v_{d\_pe}(t) = R_{pe}i_{d\_pe}(t) + L_{pe}\dfrac{di_{d\_pe}(t)}{dt} - \omega_{pe}L_{pe}i_{q\_pe}(t) \\ v_{q\_pe}(t) = R_{pe}i_{q\_pe}(t) + L_{pe}\dfrac{di_{q\_pe}(t)}{dt} \\ \qquad\qquad +\omega_{pe}\left(L_{pe}i_{d\_pe}(t) + \phi_m\right) \end{cases} \tag{19}$$

where v_{d_pe} and v_{q_pe} are the d- and q-axis armature voltages, respectively, i_{d_pe} and i_{q_pe} are the d- and q-axis armature currents, respectively, R_{pe} is the armature resistance, and L_{pe} is the armature inductance, ω_{pe} is the electrical angular frequency, and ϕ_m is the flux linking of the permanent magnet.

Considering that the armature current of the pre-exciter is pretty small, i.e., $i_{d\_pe} \approx 0$ and $i_{q\_pe} \approx 0$, we could obtain $v_{d\_pe} \approx 0$ and $v_{q\_pe} \approx \omega_{pe}\phi_m$ from (19). Thus, the output voltage of the three-phase rectification bridge can be approximated as

$$v_{dc\_rb}(t) \approx \sqrt{3}v_{q\_pe}(t) = \sqrt{3}\omega_{pe}\phi_m \tag{20}$$

where ϕ_m is constant, and ω_{pe} is mainly determined by the rotation speed of the VFAC-TSG.

The average output voltage of the chopper circuit is

$$v_{o\_cc}(t) = v_{dc\_rb}(t)d_y(t). \tag{21}$$

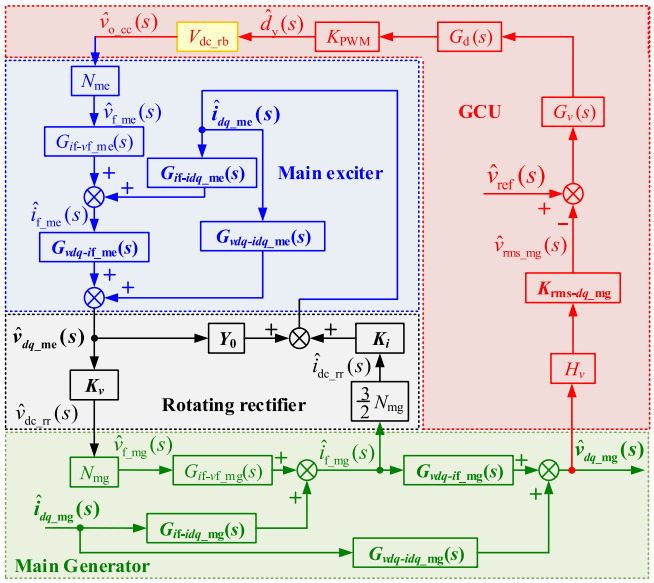

Fig. 6. Small-signal model of the VFAC-TSG.

Imposing small-signal perturbation to the variables v_{o_cc} and d_y in (21), respectively, yields

$$\hat{v}_{o\_cc}(s) = V_{dc\_rb}\hat{d}_y(s) \tag{22}$$

where V_{dc_rb} is the steady-state value of v_{dc_rb}.

The rms value v_{rms_mg} can be expressed as

$$v_{rms\_mg}(t) = \sqrt{\left(v_{d\_mg}^2(t) + v_{q\_mg}^2(t)\right)/2}. \tag{23}$$

Imposing small-signal perturbation to the variables v_{rms_mg}, v_{d_mg}, and v_{q_mg} in (23) gives

$$\hat{v}_{rms\_mg}(s) = \boldsymbol{K}_{\mathbf{rms-dq\_mg}}\hat{\boldsymbol{v}}_{\boldsymbol{dq\_mg}}(\boldsymbol{s}) \tag{24}$$

where

$$\boldsymbol{K}_{\mathbf{rms-dq\_mg}} = \begin{bmatrix} \frac{V_{d\_mg}}{2V_{rms\_mg}} & \frac{V_{q\_mg}}{2V_{rms\_mg}} \end{bmatrix} \tag{25}$$

with V_{d_mg}, V_{q_mg}, and V_{rms_mg} being the steady-state values.

A PI regulator can be adopted as $G_v(s)$, expressed as

$$G_v(s) = K_p + \frac{K_i}{s} \tag{26}$$

where K_p and K_i are the proportional and integral coefficients of the PI regulator, respectively.

D. Impedance Model of the VFAC-TSG

Integrating the separate models of the above five parts yields Fig. 6. Therein, the small-signal models of the main generator, main exciter, and rotating rectifier are coupled. For better clarity, Fig. 6 is further evolved into Fig. 7, where $G_{rr\text{-}me}(s)$ and $G_{cp}(s)$ are expressed as (27) and (28), shown at the bottom of the next page, respectively. Therein, $\boldsymbol{I}$ represents the second-order identity matrix, the subscripts "mg" and "me" represent the main generator and the main exciter, respectively, and N_{mg} and N_{me} are the ratio of the armature winding to the field winding in the main generator and the main exciter, respectively.

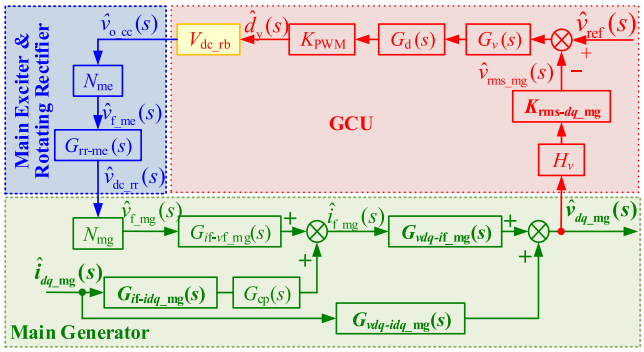

Fig. 7. Equivalent small-signal model of the VFAC-TSG.

Based on Fig. 7, the open-loop and closed-loop impedances of the VFAC-TSG, denoted as $\boldsymbol{Z_o}$ and $\boldsymbol{Z_c}$, respectively, are derived as follows. It is known that the small-signal model of the impedance represents the voltage response when the current is perturbed. The rotation speed is controlled independently of the electric circuit circumstances and thus in most cases is assumed to be constant in the modeling process [35], [36].

In the open-loop mode, $d_{\rm y}$ is fixed, i.e., $\hat{d}_{\rm y}=0$. Accordingly, $\boldsymbol{Z_o}$ is derived as

$$\boldsymbol{Z_o}(\boldsymbol{s}) = \boldsymbol{G_{vdq-if\_mg}}(\boldsymbol{s})\boldsymbol{G_{if-idq\_mg}}(\boldsymbol{s})G_{\rm cp}(s) + \boldsymbol{G_{vdq-idq\_mg}}(\boldsymbol{s}). \tag{29}$$

Substituting (6)–(8) into (29), yields

$$\boldsymbol{Z_o}(\boldsymbol{s}) = \begin{bmatrix} Z_{\rm o\_dd}(s) & Z_{\rm o\_dq}(s) \\ Z_{\rm o\_qd}(s) & Z_{\rm o\_qq}(s) \end{bmatrix} = \begin{bmatrix} R_{\rm a\_mg}+sL_{d\_mg}-G_{\rm cp}(s)\frac{s^2L^2_{md\_mg}}{R_{\rm f\_mg}+sL_{\rm f\_mg}} & -\omega_{\rm mg}L_{q\_mg} \\ \omega_{\rm mg}L_{d\_mg}-G_{\rm cp}(s)\frac{s\omega_{\rm mg}L^2_{md\_mg}}{R_{\rm f\_mg}+sL_{\rm f\_mg}} & R_{\rm a\_mg}+sL_{q\_mg} \end{bmatrix}. \tag{30}$$

In the closed-loop mode, the impedance $\boldsymbol{Z_c}$ is

$$\boldsymbol{Z_c}(\boldsymbol{s}) = (\boldsymbol{I}+\boldsymbol{T}(\boldsymbol{s}))^{-1}\boldsymbol{Z_o}(\boldsymbol{s}) \tag{31}$$

where

$$\boldsymbol{T}(\boldsymbol{s}) = \boldsymbol{G_{vdq-if\_mg}}(\boldsymbol{s})\boldsymbol{K_{rms-dq\_mg}} \frac{2V_{\rm rms\_mg}T_{\rm GCU}(s)}{(sV_{d\_mg}+\omega_{\rm mg}V_{q\_mg})L_{md\_mg}} \tag{32}$$

with $T_{\rm GCU}(s)$ being the control loop gain of the GCU, expressed as follows: (33), as shown at the bottom of this page.

Substituting (29) into (31), the expression of $\boldsymbol{Z_c}(\boldsymbol{s})$ can be derived, as shown in the following equation: where

$$G_{dd}(s) = \frac{1+\frac{\omega_{\rm mg}V_{q\_mg}}{sV_{d\_mg}+\omega_{\rm mg}V_{q\_mg}}T_{\rm GCU}(s)}{1+T_{\rm GCU}(s)} \tag{35}$$

$$G_{dq}(s) = -\frac{sV_{q\_mg}T_{\rm GCU}(s)}{(sV_{d\_mg}+\omega_{\rm mg}V_{q\_mg})(1+T_{\rm GCU}(s))} \tag{36}$$

$$G_{qd}(s) = -\frac{\omega_{\rm mg}V_{d\_mg}T_{\rm GCU}(s)}{(sV_{d\_mg}+\omega_{\rm mg}V_{q\_mg})(1+T_{\rm GCU}(s))} \tag{37}$$

$$G_{qq}(s) = \frac{1+\frac{sV_{d\_mg}}{sV_{d\_mg}+\omega_{\rm mg}V_{q\_mg}}T_{\rm GCU}(s)}{1+T_{\rm GCU}(s)} \tag{38}$$

IV. Terminal Characteristics of the VFAC-TSG

Based on the small-signal impedance model of the VFAC-TSG, its terminal characteristics in the open-loop and closed-loop modes are unfolded, and the impacts of the rotation speed and digital control delay on the terminal characteristics are further revealed in this section.

A. Open-Loop Terminal Characteristics

According to (30), $\boldsymbol{Z_o}(\boldsymbol{s})$ is a 2×2 matrix. Therein, Z_{dd} represents the voltage response in the d-axis when the d-axis current is perturbed. Z_{qq} represents the q-axis voltage response when q-axis current is perturbed. Z_{dq} and Z_{qd} represent the coupling effect between the d- and q-axes. As observed from (30), $Z_{\rm o\_dd}$ and $Z_{\rm o\_qq}$ are dominated by the impedance of the main generator. With the parameters in Appendix, and according to (30), the frequency plots of $Z_{\rm o\_dd}$, $Z_{\rm o\_qq}$, $Z_{\rm o\_dq}$, and $Z_{\rm o\_qd}$ can be depicted, as shown in Fig. 8, where the range of frequency is up to the Nyquist frequency.

As can be observed from Fig. 8, $Z_{\rm o\_dd}(s)$ and $Z_{\rm o\_qq}(s)$ are dominated by $R_{\rm a\_mg}$ in the low frequency range, featuring as a resistance. As the frequency increases, the effects of sL_{d_mg} and sL_{q_mg} become dominant, and thus $Z_{\rm o\_dd}(s)$ and $Z_{\rm o\_qq}(s)$ are inductive. Besides, the amplitudes of $Z_{\rm o\_dq}(s)$ and $Z_{\rm o\_qd}(s)$ are larger than those of $Z_{\rm o\_dd}(s)$ and $Z_{\rm o\_qq}(s)$ in the most frequency range, so the coupling effect between the d- and q-axes is significant.

$$G_{\rm rr-me}(s) = G_{\rm cp}(s)\boldsymbol{K_v}(\boldsymbol{I}-(\boldsymbol{G_{vdq-if\_me}}(\boldsymbol{s})\boldsymbol{G_{if-idq\_me}}(\boldsymbol{s})+\boldsymbol{G_{vdq-idq\_me}}(\boldsymbol{s}))\boldsymbol{Y_0})^{-1}\boldsymbol{G_{vdq-if\_me}}(\boldsymbol{s})G_{\rm if-vf\_me}(s) \tag{27}$$

$$G_{\rm cp}(s) = \frac{1}{1-\frac{3}{2}\left(G_{\rm if-vf\_mg}(s)N_{\rm mg}\boldsymbol{K_v}(\boldsymbol{I}-(\boldsymbol{G_{vdq-if\_me}}(\boldsymbol{s})\boldsymbol{G_{if-idq\_me}}(\boldsymbol{s})+\boldsymbol{G_{vdq-idq\_me}}(\boldsymbol{s}))\boldsymbol{Y_0})^{-1}(\boldsymbol{G_{vdq-if\_me}}(\boldsymbol{s})\boldsymbol{G_{if-idq\_me}}(\boldsymbol{s})+\boldsymbol{G_{vdq-idq\_me}}(\boldsymbol{s}))\boldsymbol{K_i}N_{\rm me}\right)} \tag{28}$$

$$T_{\rm GCU}(s) = \frac{(sV_{d\_mg}+\omega_{\rm mg}V_{q\_mg})L_{md\_mg}N_{\rm me}G_{\rm rr-me}(s)G_{\rm d}(s)V_{\rm dc\_rb}K_{\rm PWM}G_v(s)N_{\rm mg}H_v}{2V_{\rm rms\_mg}(R_{\rm f\_mg}+sL_{\rm f\_mg})}. \tag{33}$$

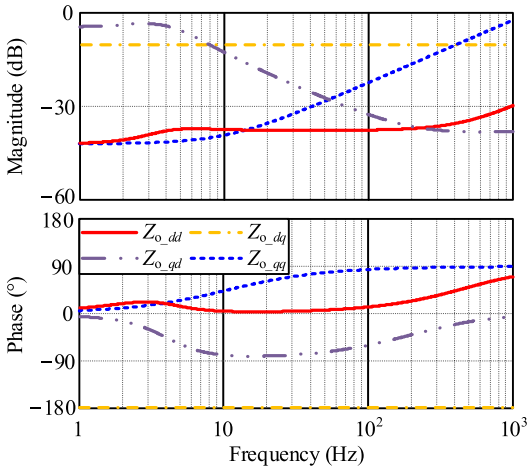

Fig. 8. Frequency plots of $Z_o(s)$.

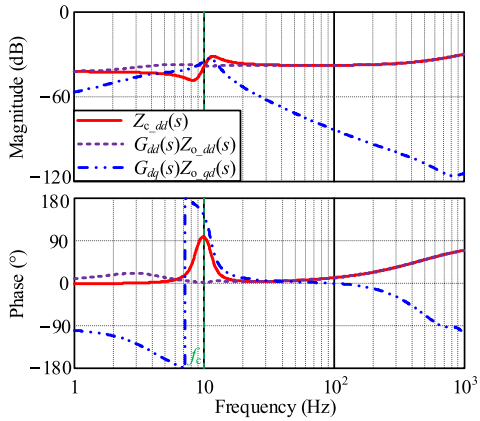

Fig. 9. Bode plots of $Z_{c\_dd}(s)$.

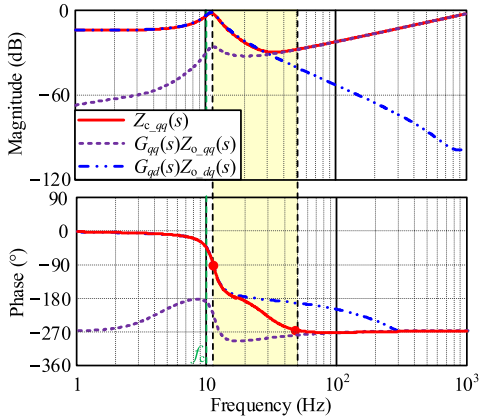

Fig. 10. Bode plots of $Z_{c\_qq}(s)$.

TABLE I
PARAMETERS OF THE VFAC-TSG

Symbol	Parameter	Low-Speed Mode	High-Speed Mode
ω_{mg}	Line frequency of MG	2π×400 rad/s	2π×800 rad/s
V_{d_mg}	*d*-axis armature voltage of MG	89.8 V	129.5 V
V_{q_mg}	*q*-axis armature voltage of MG	135.6 V	97.8 V
H_v	Voltage sensor gain	1	1
K_p	Proportional gain of $G_v(s)$	0.01	0.01
K_i	Integral gain of $G_v(s)$	0.05	0.05
ω_{me}	Line frequency of ME	2π×666.7 rad/s	2π×1333.4 rad/s
δ_N	Power angle of ME	0.89 rad	1.12 rad
V_{d_me}	*d*-axis armature voltage of ME	21.97 V	21.94 V
V_{q_me}	*q*-axis armature voltage of ME	17.86 V	10.87 V
I_{d_me}	*d*-axis armature current of ME	17.81 A	16.88 A
I_{q_me}	*q*-axis armature current of ME	10.64 A	5.3 A
ω_{pe}	Line frequency of PE	2π×800 rad/s	2π×1600 rad/s
f_{sw}	Switching frequency	2 kHz	2 kHz
f_s	Sampling frequency	2 kHz	2 kHz

B. Closed-Loop Terminal Characteristics

Recalling (34), shown at the bottom of this page, $\mathbf{Z_c}(s)$ is also a 2×2 matrix. The characteristics of $Z_{c\_dd}(s)$ and $Z_{c\_qq}(s)$ are studied in the following.

Table I lists the steady-state parameters of the VFAC-TSG under the low-speed and high-speed conditions. Substituting the parameters in Table I and Appendix into (34), the Bode plots of $Z_{c\_dd}(s)$ and $Z_{c\_qq}(s)$ are depicted, as shown in Figs. 9 and 10, respectively. As shown, both $Z_{c\_dd}(s)$ and $Z_{c\_qq}(s)$ have one magnitude peak around the cutoff frequency of $T_{GCU}(s)$, which is denoted as f_c. The characteristics of $Z_{c\_dd}(s)$ and $Z_{c\_qq}(s)$ in the frequency range of $(0, f_c)$ and $(f_c, f_s/2)$ are sequentially studied as follows.

1) $Z_{c\_dd}(s)$ in the Frequency Range of $(0, f_c)$: As shown in (34), $Z_{c\_dd}(s) = G_{dd}(s)Z_{o\_dd}(s) + G_{dq}(s)Z_{o\_qd}(s)$. Generally, the inertia of the VFAC-TSG is strong, f_c is far lower than the fundamental frequency of the VFAC-TSG, so we have $sV_{d\_mg} + \omega_{mg}V_{q\_mg} \approx \omega_{mg}V_{q\_mg}$ in the frequency range of $(0, f_c)$. Besides, considering that $|T_{GCU}(s)|$ is high in $(0, f_c)$, we also have $T_{GCU}(s) \approx 1 + T_{GCU}(s)$. Substituting them into (35) and (36), respectively, $G_{dd}(s)$ and $G_{dq}(s)$ are approximated as

$$G_{dd}(s) \approx 1 \tag{39}$$

$$G_{dq}(s) \approx -s/\omega_{mg}. \tag{40}$$

Accordingly, $G_{dd}(s)Z_{o\_dd}(s) \approx Z_{o\_dd}(s)$ holds, and $G_{dq}(s)Z_{o\_qd}(s)$ can be simplified as

$$G_{dq}(s)Z_{o\_qd}(s) \approx -\frac{s}{\omega_{mg}}Z_{o\_qd}(s) \approx -\frac{sL_{d\_mg}R_{f\_mg}}{R_{f\_mg} + sL_{f\_mg}}. \tag{41}$$

$$\boldsymbol{Z_c}(s) = \begin{bmatrix} Z_{c\_dd}(s) & Z_{c\_dq}(s) \\ Z_{c\_qd}(s) & Z_{c\_qq}(s) \end{bmatrix} = \begin{bmatrix} G_{dd}(s)Z_{o\_dd}(s) + G_{dq}(s)Z_{o\_qd}(s) & G_{dd}(s)Z_{o\_dq}(s) + G_{dq}(s)Z_{o\_qq}(s) \\ G_{qd}(s)Z_{o\_dd}(s) + G_{qq}(s)Z_{o\_qd}(s) & G_{qd}(s)Z_{o\_dq}(s) + G_{qq}(s)Z_{o\_qq}(s) \end{bmatrix} \tag{34}$$

Recalling the analysis in Section IV-A, Z_{o_dd} is dominated by R_{a_mg} in the low frequency range. Thus, $G_{dd}(s)Z_{o\_dd}(s)$ is resistive in this case. According to (41), $G_{dq}(s)Z_{o\_qd}(s)$ is negatively resistive–inductive. These conclusions are identical to Fig. 9. Besides, as shown in Fig. 9, in $(0, f_c)$, the magnitude of $G_{dq}(s)Z_{o\_qd}(s)$ is lower than that of $G_{dd}(s)Z_{o\_dd}(s)$, and the phase difference between $G_{dq}(s)Z_{o\_qd}(s)$ and $G_{dd}(s)Z_{o\_dd}(s)$ is greater than 90°. Thus, $Z_{c\_dd}(s)$, as the sum of them, whose magnitude is lower than that of $Z_{o\_dd}(s)$ and is mainly resistive in $(0, f_c)$ (see Fig. 9).

2) $Z_{c\_dd}(s)$ in the Frequency Range of (f_c, f_s/2): By taking the dominant terms, the expressions of $G_{dd}(s)$ and $G_{dq}(s)$ at the frequencies higher than f_c can be approximated as

$$G_{dd}(s) \approx 1 \tag{42}$$

$$G_{dq}(s) \approx -\frac{s}{\omega_{mg}} T_{GCU}(s) \tag{43}$$

Accordingly, $G_{dd}(s)Z_{o\_dd}(s) \approx Z_{o\_dd}(s)$ still holds. Combining (33) and (43), the characteristics of $G_{dq}(s)$ in this frequency range feature the first-order low-pass characteristic. Recalling that $Z_{o\_qd}(s)$ also features the first-order low-pass characteristic, the amplitude of $G_{dq}(s)$ $Z_{o\_qd}(s)$ is far less than that of $Z_{o\_dd}(s)$ in (f_c,f_s/2), as shown in Fig. 9. Thus, as the sum of them, $Z_{c\_dd}(s)$ is similar with $Z_{o\_dd}(s)$ and is resistive–inductive in (f_c,f_s/2) (see Fig. 9).

3) $Z_{c\_qq}(s)$ in the Frequency Range of (0, f_c): Likewise, taking the dominant terms, $G_{qd}(s)Z_{o\_dq}(s)$ and $G_{qq}(s)$ in the frequency range of $(0, f_c)$ are simplified as

$$G_{qd}(s)Z_{o\_dq}(s) \approx V_{d\_mg}\omega_{mg}L_{q\_mg}/V_{q\_mg} \tag{44}$$

$$G_{qq}(s) \approx \frac{1}{T_{GCU}(s)}. \tag{45}$$

According to (44) and (45), and considering that $|T_{GCU}(s)|$ is high in $(0, f_c)$, $Z_{c\_qq}(s) = G_{qd}(s)Z_{o\_dq}(s) + G_{qq}(s)Z_{o\_qq}(s)$ can be approximated as

$$Z_{c\_qq}(s) \approx G_{qd}(s)Z_{o\_dq}(s) \approx V_{d\_mg}\omega_{mg}L_{q\_mg}/V_{q\_mg}. \tag{46}$$

Observing (46), $Z_{c\_qq}(s)$ features as resistance in this frequency range, as shown in Fig. 10. Besides, its amplitude depends on the relation between V_{d_mg} and V_{q_mg}. Defining the ratio of V_{d_mg} and V_{q_mg} as λ, since $Z_{o\_qq}(s) \approx R_{a\_mg}$ holds in this frequency range, the condition for $|Z_{c\_qq}(s)| > |Z_{o\_qq}(s)|$ is

$$\lambda = \frac{V_{d\_mg}}{V_{q\_mg}} \geq \frac{R_{a\_mg}}{\omega_{mg}L_{q\_mg}} \triangleq \lambda_{cri} \tag{47}$$

where $\lambda_{cri} = R_{a\_mg}/\omega_{mg}L_{q\_mg}$ is the critical value of V_{d_mg}/V_{q_mg}.

For better clarity, the Bode plots of $Z_{c\_qq}(s)$ with different λ were depicted in Fig. 11. As shown, in $(0, f_c)$, $|Z_{c\_qq}(s)| < R_{a\_mg}$ is valid only under $\lambda < \lambda_{cri}$, which is in agreement with the above analysis.

Besides, as shown in Fig. 11, there is a special case, i.e., $\lambda = 0$, where the phase of $Z_{c\_qq}(s)$ approaches 90° in $(0, f_c)$. This is because $G_{qd}(s)Z_{o\_dq}(s) = 0$ holds in this case, leading to $Z_{c\_qq}(s) = G_{qq}(s)Z_{o\_qq}(s) \approx Z_{o\_qq}(s)/T_{GCU}(s)$ instead of (46).

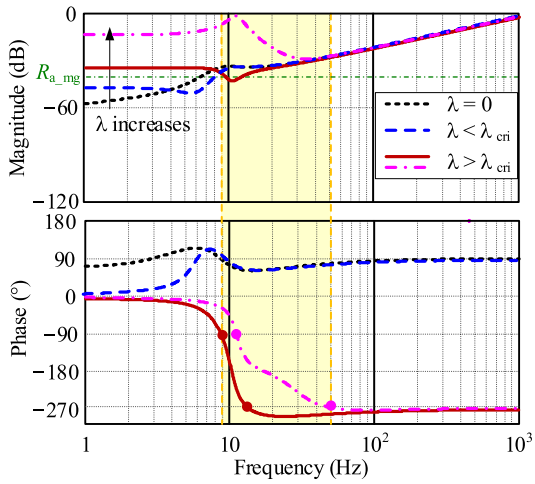

Fig. 11. Bode plots of $Z_{c\_qq}(s)$ with different λ.

Since $Z_{o\_qq}(s)$ approximately features as resistance in $(0, f_c)$, the feature of $Z_{c\_qq}(s)$ is opposite to that of $T_{GCU}(s)$. According to (33), $T_{GCU}(s)$ features second-order low-pass characteristic and tends to be capacitive in low frequency range. Therefore, $Z_{c\_qq}(s)$ tends to be inductive in $(0, f_c)$.

4) $Z_{c\_qq}(s)$ in the Frequency Range of (f_c, f_s/2): Likewise, the expressions of $G_{qd}(s)Z_{o\_dq}(s)$ and $G_{qq}(s)$ in the frequency range of (f_c, f_s/2) are simplified as

$$G_{qd}(s)Z_{o\_dq}(s) \approx \frac{V_{d\_mg}\omega_{mg}L_{q\_mg}}{V_{q\_mg}} T_{GCU}(s) \tag{48}$$

$$G_{qq}(s) \approx 1. \tag{49}$$

Accordingly, $G_{qq}(s)Z_{o\_qq}(s) \approx Z_{o\_qq}(s)$ holds. Observing (48), the characteristic of $G_{qd}(s)Z_{o\_dq}(s)$ in (f_c, f_s/2) is also determined by the ratio of V_{d_mg} and V_{q_mg}, i.e., λ.

When $\lambda < \lambda_{cri}$, $Z_{c\_qq}(s)$ is dominated by $Z_{o\_qq}(s)$, featuring resistive–inductive. Otherwise, the initial amplitude of $G_{qd}(s)Z_{o\_dq}(s)$ is larger than that of $G_{qq}(s)Z_{o\_qq}(s)$. Since the amplitude of $G_{qd}(s)Z_{o\_dq}(s)$ attenuates with a slope of −40 dB/dec and the amplitude of $G_{qq}(s)Z_{o\_qq}(s)$ increases with a slope of 20 dB/dec, there is an intersection between them (see Fig. 10). At the frequencies below the intersection frequency, $Z_{c\_qq}(s)$ is dominated by $G_{qd}(s)Z_{o\_dq}(s)$, featuring as a negative resistor-capacitance. At the frequencies above the intersection frequency, $Z_{c\_qq}(s)$ is dominated by $G_{qq}(s)Z_{o\_qq}(s)$ and gradually changed to inductive. Besides, the negative resistance frequency range of $Z_{c\_qq}(s)$ becomes wider with the increase of λ (see Fig. 11).

C. Impacts of the Rotation Speed

The main generator, main exciter, and pre-exciter are all connected in the same transmission shaft of the engine, so ω_{mg}, ω_{me}, and ω_{pe} are synchronously determined by the rotation speed. As mentioned, the rotation speed varies in a wide range of practical applications, which have an impact on the terminal characteristics.

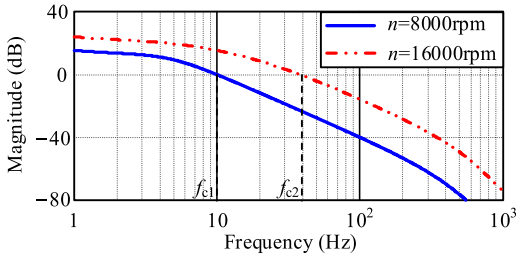

Fig. 12. Magnitude plots of $T_{\mathrm{GCU}}(s)$ under different rotation speeds.

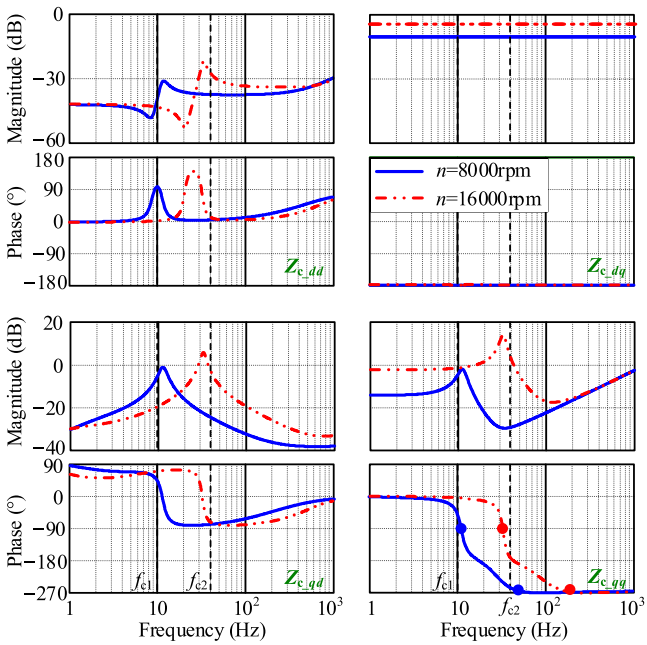

Fig. 13. Bode plots of $\mathbf{Z_c}(s)$ under different rotation speeds.

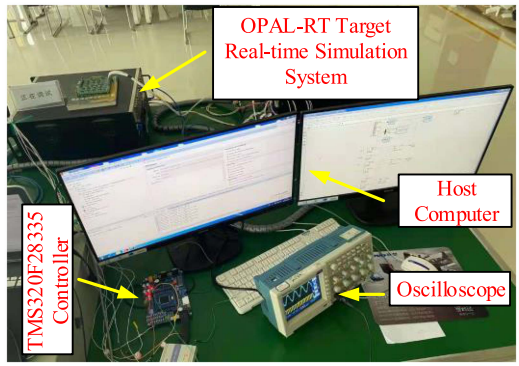

Fig. 14. Hardware-in-the-loop platform.

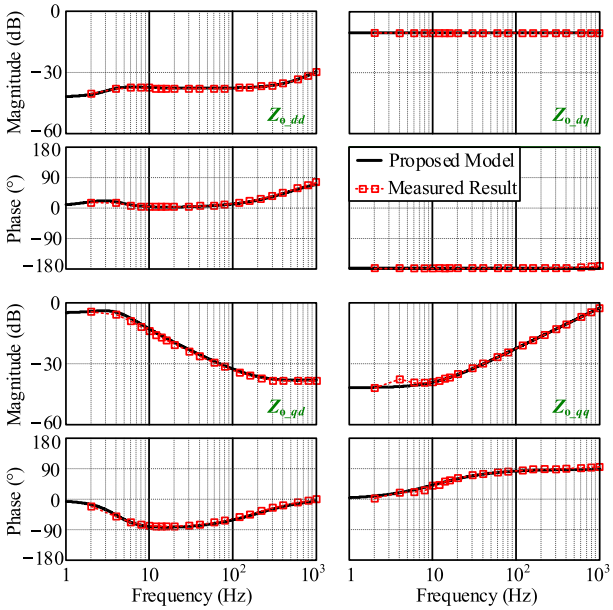

Fig. 15. Measured result compared with the proposed model for $Z_{\mathrm{o}}(s)$.

According to (30), the amplitudes of $Z_{\mathrm{o}\_dq}(s)$ and $Z_{\mathrm{o}\_qd}(s)$ increase as ω_{mg} increases, which indicates that the coupling between d and q axes becomes more significant. Besides, with the increase of the rotation speed, the gain of $T_{\mathrm{GCU}}(s)$ increases and, thus, f_{c} goes higher. This can be verified by depicting the magnitude plot of $T_{\mathrm{GCU}}(s)$ with the parameters in Table I and Appendix, as shown in Fig. 12.

Substituting the parameters in Table I and Appendix into (33), the Bode plots of $\mathbf{Z_c}(s)$ under low-speed and high-speed can also be depicted, as shown in Fig. 13. As can be observed, a higher rotation speed shifts the magnitude peaks of Z_{c_dd}, Z_{c_qd}, and Z_{c_qq} toward high-frequency regions, and increases the magnitude of Z_{c_dq}. Besides, the negative resistance frequency range of Z_{c_qq} becomes wider.

D. Impacts of the Digital Control Delay

According to the expression of the $G_{\mathrm{d}}(s)$, the phase lag caused by the digital control delay in the low frequency range is quite small. Considering that f_{c} is low, the impacts of the digital control delay on $\mathbf{Z_c}(s)$ in $(0, f_{\mathrm{c}})$ can be ignored. Furthermore, according to the analysis in Section IV-B, the approximate expressions of $Z_{\mathrm{c}\_dd}(s)$ and $Z_{\mathrm{c}\_qq}(s)$ in $(f_{\mathrm{c}}, f_{\mathrm{s}}/2)$ do not contain $G_{\mathrm{d}}(s)$, which thus will not pose an impact on the characteristic of $\mathbf{Z_c}(s)$. Overall, the impacts of the digital control delay on $\mathbf{Z_c}(s)$ can be ignored.

V. Experimental Verification

To verify the accuracy of the established small-signal impedance model and the correctness of the theoretical analysis, experiments are performed based on the hardware-in-the-loop platform, as shown in Fig. 14. The model of the VFAC-TSG and the module of the disturbance signal generation are implemented on the OPAL-RT Target Real-time Simulation System, and the voltage controller of the GCU is implemented in a TMS320F28335 DSP. The output voltage and current of the VFAC-TSG are measured by the oscilloscope. The parameters for these experiments are listed in Table I and Appendix.

The first set of experiments is conducted to verify the accuracy of the proposed impedance model. The results of the open-loop and closed-loop impedances are shown in Figs. 15 and 16, respectively. As can be observed, the proposed open-loop and closed-loop impedance model always matches well with

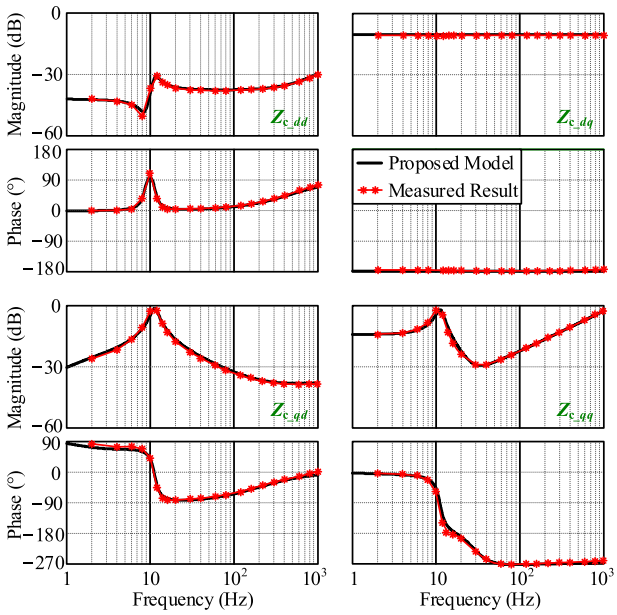

Fig. 16. Measured result compared with the proposed model for $Z_{\mathrm{c}}(s)$.

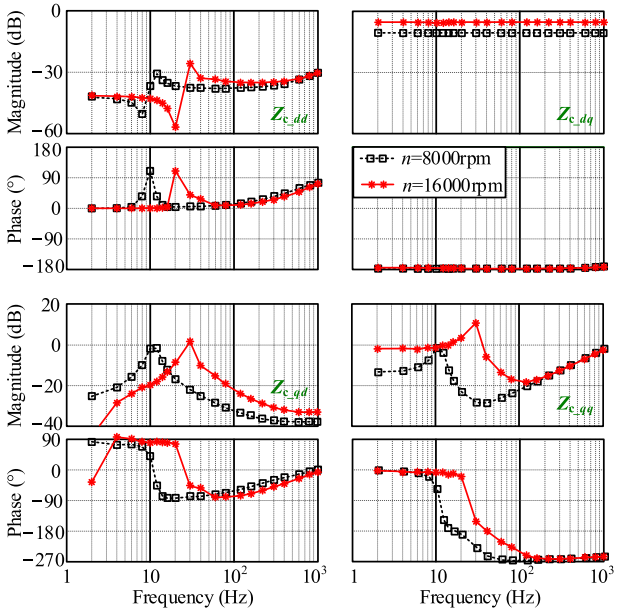

Fig. 17. Measured results for $Z_{\mathrm{c}}(s)$ under different rotation speeds.

the measurement, which confirms that the proposed impedance model is accurate.

The second set of experiments is conducted to confirm the theoretical analysis in Section IV. Fig. 17 shows the measured results of $\boldsymbol{Z_{\mathrm{c}}(s)}$ under different rotation speeds. As can be observed, with the increase in rotation speed, the magnitude peaks of $Z_{\mathrm{c\_}dd}$, $Z_{\mathrm{c\_}qd}$ and $Z_{\mathrm{c\_}qq}$ move toward high-frequency regions, the magnitude of $Z_{\mathrm{c\_}dq}$ increases, and the negative resistance frequency range of $Z_{\mathrm{c\_}qq}$ becomes wider. The results are consistent with the results shown in Fig. 13, and confirm that the theoretical analysis regarding the impact of the rotation speed on the terminal characteristics is correct.

VI. Conclusion

This article established an accurate small-signal impedance model of the VFAC-TSG under the synchronous *d-q* frame. On this basis, the open-loop and closed-loop terminal characteristics of the VFAC-TSG were thoroughly analyzed. It was found that the characteristics of the open-loop impedances (i.e., $Z_{\mathrm{o\_}dd}$ and $Z_{\mathrm{o\_}qq}$) are resistive in low frequency range and gradually change to inductive in high frequency range. The closed-loop impedances (i.e., $Z_{\mathrm{c\_}dd}$ and $Z_{\mathrm{c\_}qq}$) had a magnitude peak located around the cutoff frequency of T_{GCU}. Besides, $Z_{\mathrm{c\_}qq}$ presented the negative resistance characteristic once the ratio of *d*-axis and *q*-axis armature voltages of the main generator exceeded its critical value.

Furthermore, the impacts of rotation speed variation on the terminal characteristics were studied. As the rotation speed increased, the frequencies of the magnitude peaks of $Z_{\mathrm{c\_}dd}$ and $Z_{\mathrm{c\_}qq}$ became higher, the negative resistance frequency range of $Z_{\mathrm{c\_}qq}$ became wider, and the coupling between *d* and *q* axes became stronger. The impact of the digital control delay on $\boldsymbol{Z_{\mathrm{c}}(s)}$ could be ignored.

The accuracy of the established impedance model and the correctness of the theoretical analysis were finally verified by the experiments on the hardware-in-the-loop platform. The impedance model and the above findings provided theoretical support for the future work on the stability analysis and parameter optimization of the MEA VFAC power system.

Appendix

The parameters of the VFAC-TSG are presented in this Appendix, which are illustrated as follows.

1) *Main generator*: 6 poles, Smg = 90 kVA, Ra_mg = 8 mΩ, Ll_mg = 1.15 μH, Lmd_mg = 0.23 mH, Lmq_mg = 0.12 mH, Rf_mg = 2.78 mΩ, Llf_mg = 3.32 μH, and Nmg = 0.029.
2) *Main exciter*: 10 poles, Sme = 2.07 kVA, Ra_me = 0.07 Ω, Ll_me = 0.25 mH, Lmd_me = 0.42 mH, Lmq_me = 0.27 mH, Rf_me = 5.59 mΩ, Llf_me = 0.06 μH, and Nme = 0.036.
3) *Pre-exciter*: 12 poles, Spe = 0.35 kVA, Rpe = 0.3 Ω, Lpe = 0.27 mH, and ϕm = 0.0046 Wb.

References

[1] G. Buticchi, S. Bozhko, M. Liserre, P. Wheeler, and K. Al-Haddad, "On-board microgrids for the more electric aircraft–Technology review," *IEEE Trans. Ind. Electron.*, vol. 66, no. 7, pp. 5588–5599, Jul. 2019.
[2] B. Sarlioglu and C. T. Morris, "More electric aircraft: Review, challenges, and opportunities for commercial transport aircraft," *IEEE Trans. Transp. Electrific.*, vol. 1, no. 1, pp. 54–64, Jun. 2015.
[3] I. Moir, *Aircraft Systems: Mechanical, Electrical, and Avionics Subsystems Integration*, 3rd ed. Chichester, U.K.: Wiley, 2008.
[4] V. Madonna, P. Giangrande, and M. Galea, "Electrical power generation in aircraft: Review, challenges, and opportunities," *IEEE Trans. Transp. Electrific.*, vol. 4, no. 3, pp. 646–659, Sep. 2018.
[5] A. Abdel-Hafez, *Power Generation and Distribution System for a More Electric Aircraft—A Review*. Rijeka, Croatia: IntechOpen, 2012.
[6] Z. Zhang, J. Li, Y. Liu, Y. Xu, and Y. Yan, "Overview and development of variable frequency ac generators for more electric aircraft generation system," *Chin. J. Elect. Eng.*, vol. 3, no. 2, pp. 32–40, Sep. 2017.
[7] P. Wheeler and S. Bozhko, "The more electric aircraft: Technology and challenges," *IEEE Electrific. Mag.*, vol. 2, no. 4, pp. 6–12, Dec. 2014.

[8] K. Rajashekara, "More electric aircraft trends [technology leaders]," *IEEE Electrific. Mag.*, vol. 2, no. 4, pp. 4–39, Dec. 2014.
[9] J. Chen, C. Wang, and J. Chen, "Investigation on the selection of electric power system architecture for future more electric aircraft," *IEEE Trans. Transp. Electrific.*, vol. 4, no. 2, pp. 563–576, Jun. 2018.
[10] X. Roboam, B. Sareni, and A. D. Andrade, "More electricity in the air: Toward optimized electrical networks embedded in more-electrical aircraft," *IEEE Ind. Electron. Mag.*, vol. 6, no. 4, pp. 6–17, Dec. 2012.
[11] N. Jiao, W. Liu, J. Peng, S. Mao, and H. Zhang, "Design and control strategy of a two-phase brushless exciter for three-stage starter/generator," in *Proc. IEEE Energy Convers. Congr. Expo.*, 2014, pp. 5864–5869.
[12] K. Ni et al., "Electrical and electronic technologies in more-electric aircraft: A review," *IEEE Access*, vol. 7, pp. 76145–76166, 2019.
[13] X. Zhang, Q. Zhong, and W. Ming, "Stabilization of a cascaded dc converter system via adding a virtual adaptive parallel impedance to the input of the load converter," *IEEE Trans. Power Electron.*, vol. 31, no. 3, pp. 1826–1832, Mar. 2016.
[14] A. Riccobono and E. Santi, "Comprehensive review of stability criteria for dc power distribution systems," *IEEE Trans. Ind. Appl.*, vol. 50, no. 5, pp. 3525–3535, Sep. 2014.
[15] B. Karanayil, M. Ciobotaru, and V. G. Agelidis, "Power flow management of isolated multiport converter for more electric aircraft," *IEEE Trans. Power Electron.*, vol. 32, no. 7, pp. 5850–5861, Jul. 2017.
[16] A. Barzkar and M. Ghassemi, "Electric power systems in more and all electric aircraft: A review," *IEEE Access*, vol. 8, pp. 169314–169332, 2020.
[17] J. Sun, "Small-signal methods for ac distributed power systems–A review," *IEEE Trans. Power Electron.*, vol. 24, no. 11, pp. 2545–2554, Nov. 2009.
[18] K.-N. Areerak, S. V. Bozhko, G. M. Asher, L. De Lillo, and D. W. P. Thomas, "Stability study for a hybrid ac–dc more-electric aircraft power system," *IEEE Trans. Aerosp. Electron. Syst.*, vol. 48, no. 1, pp. 329–347, Jan. 2012.
[19] K.-N. Areerak, T. Wu, S. V. Bozhko, G. M. Asher, and D. W. P. Thomas, "Aircraft power system stability study including effect of voltage control and actuators dynamic," *IEEE Trans. Aerosp. Electron. Syst.*, vol. 47, no. 4, pp. 2574–2589, Oct. 2011.
[20] M. K. Zadeh, R. Gavagsaz-Ghoachani, B. Nahid-Mobarakeh, S. Pierfederici, and M. Molinas, "Stability analysis of hybrid ac/dc power systems for more electric aircraft," in *Proc. IEEE Appl. Power Electron. Conf. Expo.*, 2016, pp. 446–452.
[21] T. Wu, S. V. Bozhko, G. M. Asher, and D. W. P. Thomas, "Accelerated functional modeling of aircraft electrical power systems including fault scenarios," in *Proc. 35th Annu. Conf. IEEE Ind. Electron.*, 2009, pp. 2537–2544.
[22] Q. Xu, P. Wang, J. Chen, C. Wen, and M. Y. Lee, "A module-based approach for stability analysis of complex more-electric aircraft power system," *IEEE Trans. Transp. Electrific.*, vol. 3, no. 4, pp. 901–919, Dec. 2017.
[23] B. Wen, D. Boroyevich, R. Burgos, P. Mattavelli, and Z. Shen, "Small-signal stability analysis of three-phase ac systems in the presence of constant power loads based on measured *d–q* frame impedances," *IEEE Trans. Power Electron.*, vol. 30, no. 10, pp. 5952–5963, Oct. 2015.
[24] Y. Liao, Z. Liu, H. Zhang, and B. Wen, "Low-frequency stability analysis of single-phase system with *dq*–frame impedance approach—Part I: Impedance modeling and verification," *IEEE Trans. Ind. Appl.*, vol. 54, no. 5, pp. 4999–5011, Sep./Oct. 2018.
[25] Y. Liao, Z. Liu, H. Zhang, and B. Wen, "Low-frequency stability analysis of single-phase system with *dq*–frame impedance approach—Part II: Stability and frequency analysis," *IEEE Trans. Ind. Appl.*, vol. 54, no. 5, pp. 5012–5024, Sep./Oct. 2018.
[26] B. Wen, D. Boroyevich, R. Burgos, P. Mattavelli, and Z. Shen, "Analysis of *d–q* small-signal impedance of grid-tied inverters," *IEEE Trans. Power Electron.*, vol. 31, no. 1, pp. 675–687, Jan. 2016.
[27] B. Wen, D. Dong, D. Boroyevich, R. Burgos, P. Mattavelli, and Z. Shen, "Impedance-based analysis of grid-synchronization stability for three-phase paralleled converters," *IEEE Trans. Power Electron.*, vol. 31, no. 1, pp. 26–38, Jan. 2016.
[28] F. Gao and S. Bozhko, "Modeling and impedance analysis of a single dc bus-based multiple-source multiple-load electrical power system," *IEEE Trans. Transp. Electrific.*, vol. 2, no. 3, pp. 335–346, Sep. 2016.
[29] F. Gao, S. Bozhko, A. Costabeber, G. Asher, and P. Wheeler, "Control design and voltage stability analysis of a droop-controlled electrical power system for more electric aircraft," *IEEE Trans. Ind. Electron.*, vol. 64, no. 12, pp. 9271–9281, Dec. 2017.
[30] J. Yang et al., "Modeling and stability enhancement of a permanent magnet synchronous generator based dc system for more electric aircraft," *IEEE Trans. Ind. Electron.*, vol. 69, no. 3, pp. 2511–2520, Mar. 2022.
[31] N. Su, W. Huang, and F. Bu, "Analysis of spontaneous and implicit internal self-excitation in aircraft variable frequency ac power system based on dual-stator winding induction generator," *IEEE Trans. Ind. Electron.*, vol. 69, no. 7, pp. 6657–6667, Jul. 2022.
[32] Y. Yan, *Power Supplies for Aircrafts*. Beijing, China: Aviation Ind. Press, 1995.
[33] S. D. Sudhoff and O. Wasynczuk, "Analysis and average-value modeling of line-commutated converter-synchronous machine systems," *IEEE Trans. Energy Convers.*, vol. 8, no. 1, pp. 92–99, Mar. 1993.
[34] Z. Lin, X. Ruan, H. Zhang, and L. Wu, "A generalized real-time computation method with dual-sampling mode to eliminate the computation delay in digitally controlled inverters," *IEEE Trans. Power Electron.*, vol. 37, no. 5, pp. 5186–5195, May 2022.
[35] A. Griffo and J. Wang, "Modeling and stability analysis of hybrid power systems for the more electric aircraft," *Electric. Power Syst. Res.*, vol. 82, no. 1, pp. 59–67, 2012.
[36] S. P. Rosado, "Voltage stability and control in autonomous electric power systems with variable frequency," Ph.D. dissertation, Virginia Polytech. Inst. State Univ., Blacksburg, VA, USA, 2007.

Shuang Wang (Student Member, IEEE) received the B.S. degree in electrical engineering and automation from Northeast Agricultural University, Harbin, China, in 2016, and the M.S. degree in electrical engineering from Northeastern University, Shenyang, China, in 2019. He is currently working toward the Ph.D. degree in electrical engineering with the College of Automation Engineering, Nanjing University of Aeronautics and Astronautics, Nanjing, China.

His current research interests include modeling, control, and stability of more electric aircraft power systems.

Xinbo Ruan (Fellow, IEEE) received the B.S. and Ph.D. degrees in electrical engineering from Nanjing University of Aeronautics and Astronautics, Nanjing, China, in 1991 and 1996, respectively.

In 1996, he joined the Faculty of Electrical Engineering Teaching and Research Division, Nanjing University of Aeronautics and Astronautics, where he became a Professor with the College of Automation Engineering in 2002 and was engaged in teaching and research in the field of power electronics. From August to October 2007, he was a research fellow with the Department of Electronic and Information Engineering, The Hong Kong Polytechnic University, Hong Kong, SAR China. From March 2008 to August 2011, he was also with the School of Electrical and Electronic Engineering, Huazhong University of Science and Technology, Wuhan, China. He is the author or coauthor of 13 books and more than 300 technical papers published in journals and conferences. His main research interests include resonant and soft-switching power converters, power converter topologies and control, grid-connected converters and systems for renewable energy, modeling and stability of power converters, and envelop tracking power supply.

Prof. Ruan was (from 2005 to 2013) and has been (since 2017 again) the Vice President of the China Power Supply Society. From 2014 to 2016, he was the Vice Chair of the Technical Committee on Renewable Energy Systems within the IEEE Industrial Electronics Society. He was the General Chair of IPEMC-ECCE Asia 2020 and the General Secretary of IPEMC-ECCE Asia 2009, the Technical Program Committee Chair of the IEEE 7th Annual Energy Conversion Congress and Exposition (ECCE2015), and the Tutorial Committee Chair of the IEEE 12th Annual Energy Conversion Congress and Exposition (ECCE2020). He is currently an Editor for IEEE JOURNAL OF EMERGING AND SELECTED TOPICS ON POWER ELECTRONICS and an Associate Editor for IEEE TRANSACTIONS ON INDUSTRIAL ELECTRONICS, IEEE TRANSACTIONS ON POWER ELECTRONICS, IEEE OPEN JOURNAL OF THE INDUSTRIAL ELECTRONICS SOCIETY, and IEEE TRANSACTIONS ON CIRCUITS AND SYSTEMS - II. He was a recipient of the Sustainable Energy Systems Technical Achievement Award from IEEE Power Electronics Society in 2022, the Delta Scholarship by the Delta Environment and Education Fund in 2003, and the Special Appointed Professor of the Chang Jiang Scholars Program by the Ministry of Education, China, in 2007.

Yuying He (Member, IEEE) received the B.S. degree in electrical engineering from Central South University, Changsha, China, in 2015, and the Ph.D. degree in electrical engineering from Huazhong University of Science and Technology, Wuhan, China, in 2022.

From May 2021 to May 2022, she was also with E. ON Energy Research Center, RWTH Aachen University, Aachen, Germany. Since June 2022, she has been a tenure-track Associate Professor with Hohai University, Nanjing, China. Her research interests include modeling and control of grid-connected converters, harmonics analysis and control, and stability of renewable energy generation systems.

Zhiheng Lin (Student Member, IEEE) received the B.S. degree in electrical engineering and automation in 2017 from Nanjing University of Aeronautics and Astronautics, Nanjing, China, where he is currently working toward the Ph.D. degree in electrical engineering.

His current research interests include renewable energy generation systems, stability of grid-connected inverter systems, and digital control techniques.

Mr. Lin is currently the Vice-Chair of IEEE Power Electronics Society Membership Committee—China on Young Professionals, and the Chair of IEEE PELS NUAA Student Branch Chapter.

Chengxiang Zhang (Student Member, IEEE) received the B.S. and M.S. degrees in electrical engineering from Southwest Jiaotong University, Chengdu, China, in 2015 and 2018, respectively. He is currently working toward the Ph.D. degree in electrical engineer with Nanjing University of Aeronautics and Astronautics, Nanjing, China.

His research interests include the aircraft starter/generator and modeling and stability issues of aircraft electrical power systems.

Donghua Wu received the B.S. degree in electronic engineering from North Minzu University, Yinchuan, China, in 2000.

He is currently a Senior Engineer with Aviation Key Laboratory of Science and Technology on Aerospace Power System, Shaanxi Aero Electric Co., Ltd., Xi'an, China. His research interests include starter/generators and control and stability of more electric aircraft power systems.